Hydrodynamic stability of rockets with headwall injection

Esam M. Abu-Irshaid and Joseph Majdalani[a)]
University of Tennessee Space Institute, Tullahoma, Tennessee 37388

Grégoire Casalis
ONERA-CERT, 2 Avenue Ed. Belin, B.P. 4025, 31055 Toulouse Cedex 4, France

We investigate the hydrodynamic instability of the full-length, cylindrical models of solid and hybrid rockets with headwall injection. Our baseline is the rotational incompressible flowfield proposed in a recent study (Majdalani and Vyas, "Inviscid models of the classic hybrid rocket," AIAA Paper 2004-3474). The local nonparallel approach is implemented in which the amplitude functions are assumed to be radially dependent at fixed streamwise locations. The usual singularity along the chamber axis is eliminated using Taylor series expansions. As a result, three compatibility relations are derived and substituted for the local boundary conditions along the axis. These depend on whether the tangential wave number q is 0, 1, or larger. Our rotational model is shown to exhibit a range of instability that broadens with successive increases in headwall injection. The lowest frequency below which the flow remains unconditionally stable is observed at $\omega = 28.5$ regardless of the headwall injection rate. As usual, the zeroth order tangential mode is found to be the most amplified. Using a representative headwall injection velocity for hybrid rockets, we identify a range of frequencies along which large excursions in pressure and velocity amplitudes are possible. These surges signal the presence of a resonant-like mechanism that is akin to an acoustic instability response. The most excited frequencies vary between 387 and 415 in the vicinity of the headwall. These frequencies are spatially delayed and lowered to 93.8–163.5 when the headwall injection rate is reduced to the level associated with solid rockets. For the most critical streamwise stations, these resurging wave amplitudes are quantified and shown to exhibit spectra that mimic the waterfall data acquired in acoustic instability tests. © *2007 American Institute of Physics.*
[DOI: 10.1063/1.2434797]

I. INTRODUCTION

In this study, three-dimensional linear instability theory is applied to an idealized representation of a full-length, cylindrical, hybrid rocket. The analysis also considers a full-length solid rocket motor (SRM) with reactive headwall. The local nonparallel (LNP) approach is used in which all of the nonzero components of the basic flow are retained in the viscous Navier-Stokes equations. In recent studies, Casalis and co-workers[1–4] have implemented this approach while investigating the stability of injection driven motions in both the porous channel and tube using axisymmetric or planar flow conditions; in their work, the mean flow expressions due to Taylor[5] and Culick[6] were used to describe the bulk gas motion in simulated slab and circular-port rocket motors. Their results have been corroborated by cold-flow experiments—referred to as VECLA (*Veine d'Etude de la Couche Limite Acoustique*) and VALDO (*Veine Axisymmétrique pour Limiter le Développement des Oscillations*)—and have helped to point out the critical abscissas beyond which the flow becomes unstable (see Avalon, Casalis, and Pineau[7]). These were found to occur around 5 and 3 for the planar (VECLA) and axisymmetric (VALDO) cases, respec-

tively. This investigation follows suit by applying the LNP approach to a similar geometric setting that is germane to the conventional hybrid grain shape and that of a solid propellant motor with reactive forward closure. Here the headwall is made permeable to permit the imposition of an inlet profile that observes Berman's similarity equation.[8]

The first numerical study of hydrodynamic instability in an SRM model was carried out by Varapaev and Yagodkin.[9] This was followed by several studies on flow field instability and turbulence by Beddini,[10] Beddini and Roberts,[11] and Lee and Beddini.[12,13] Totally independently, an extended investigation that included laboratory measurements and full solutions of the Navier-Stokes equations was performed by Casalis and co-workers;[1,3] this work helped to explain the effects of radial disturbances and the inconsistencies between the two available techniques: the one that relied on perturbing the primitive variables versus the one that employed the streamfunction.[10–13] Other pioneering studies include, first, those on the unsteady wave characteristics in solid rocket motors by Avalon and Comas,[14] and Vuillot and Avalon;[15] and, second, those on parietal vortex shedding and its connection to hydrodynamic instability by Vuillot,[16] Couton et al.,[17] Ugurtas et al.,[18] and Avalon et al.[7] Two excellent surveys may be found in Ugurtas et al.[19] and Fabignon et al.[20]

In a similar context, the purpose of the present analysis is to explore the hydrodynamic instability of the idealized

---

[a)]Author to whom all correspondence should be addressed. Department of Mechanical, Aerospace and Biomedical Engineering, University of Tennessee (UTSI), 411 B. H. Goethert Pkwy, MS-23, Tullahoma, TN 37388-9700. Electronic mail: drmajdalani@gmail.com
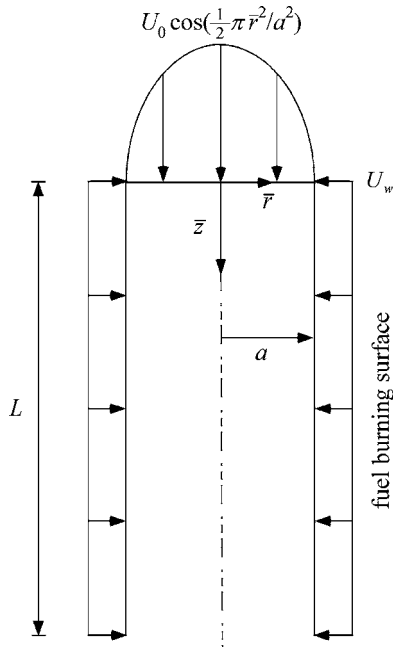
     19, 024101-1

FIG. 1. Sketch of the rotational full-length rocket model permitting mass addition along both sidewall and headwall boundaries.

solid and hybrid rockets. This will be accomplished by employing as a baseline model the core flow of the cylindrical rocket with headwall injection presented by Majdalani and Vyas.[21] Therein, two flowfield solutions were proposed, one being irrotational. In this work, the emphasis will be placed on the rotational model because of the minimal value gained from the irrotational solution.

The paper is organized as follows. In the first section, we introduce the representative mean flowfield and define its geometry. We then pursue the linear instability analysis based on small perturbations by normal mode decomposition. We implement the numerical procedure while paying particular attention to the indivisible treatment of singularity along the axis. In fact, the treatment of singularity enables us to derive the remaining boundary conditions needed to achieve closure. Next, the algorithm is verified by ensuring its ability to reproduce the same stability information for an SRM with nonreactive headwall. The corresponding flowfield is often referred to as Culick's[6] (or Taylor's[5]) and happens to be an important special case of the rotational hybrid model for which the headwall injection velocity is set to zero. After gaining confidence in the proposed methodology, results for the solid and hybrid models are presented and discussed.

II. GEOMETRY AND MEAN FLOW EQUATIONS

A. Geometry

For the hybrid core flow model mentioned above the motor is represented as a cylindrical chamber of length L and radius a (see Fig. 1). The headwall injection velocity is assumed to be Berman's cosine function with a maximum centerline velocity equal to U_0. This velocity can be adjusted to

reproduce the rate of mass addition at the injector faceplate of a hybrid rocket. On the other hand, the independent sidewall injection U_w is used to capture the regression rate of the solid fuel (Fig. 1). All coordinates are normalized by the chamber radius and velocities are normalized by U_w. In particular, the headwall injection constant is defined as $u_h = U_0/(\pi U_w)$. Note that $z=0$ stands for the upstream edge of the porous wall. The corresponding mean flow components are given by[21]

$$U_r = -\frac{1}{r}\sin\left(\frac{1}{2}\pi r^2\right),$$

$$U_z = \pi(z + u_h)\cos\left(\frac{1}{2}\pi r^2\right), \tag{1}$$

$$U_\theta = 0.$$

Before presenting the attendant analysis, it may be useful to recall that the headwall injection constant germane to hybrid rockets falls in the range of $50 \leqslant u_h \leqslant 500$.[21] At present, we start with $u_h=0$ for the purpose of providing a benchmark that can be compared to existing solutions developed for SRMs with impervious headwalls.[2] Another rotational case that is worth considering is $u_h=\frac{1}{2}$. This ratio ensures that the headwall rate of mass addition is equal to $\rho\pi a^2 U_w$, as if the headwall is allowing the same mass flux as that produced by a uniformly burning propellant placed at $z=0$. Evidently, the use of a cosine injection pattern instead of a uniform profile introduces a small error near the headwall. This error, however, quickly diminishes in the downstream direction. It follows that the validity of using a similarity-conforming cosine profile becomes more precise in a sufficiently long solid propellant grain burning equally uniformly along its headwall and sidewall.

B. Governing equations

In this problem, three-dimensional incompressible flow is treated using cylindrical coordinates; using tildes in denoting instantaneous quantities, the normalized Navier-Stokes and the continuity equations are written as:

continuity equation

$$\frac{\partial \tilde{U}_r}{\partial r} + \frac{\tilde{U}_r}{r} + \frac{1}{r}\frac{\partial \tilde{U}_\theta}{\partial \theta} + \frac{\partial \tilde{U}_z}{\partial z} = 0, \tag{2}$$

r-momentum equation

$$\frac{\partial \tilde{U}_r}{\partial t} + \tilde{U}_r\frac{\partial \tilde{U}_r}{\partial r} + \frac{\tilde{U}_\theta}{r}\frac{\partial \tilde{U}_r}{\partial \theta} - \frac{\tilde{U}_\theta^2}{r} + \tilde{U}_z\frac{\partial \tilde{U}_r}{\partial z} + \frac{\partial \tilde{P}}{\partial r}$$

$$= \frac{1}{\mathrm{Re}}\left[\frac{\partial^2 \tilde{U}_r}{\partial r^2} + \frac{1}{r}\frac{\partial \tilde{U}_r}{\partial r} - \frac{\tilde{U}_r}{r^2} + \frac{1}{r^2}\frac{\partial^2 \tilde{U}_r}{\partial \theta^2}\right.$$

$$\left. - \frac{2}{r^2}\frac{\partial \tilde{U}_\theta}{\partial \theta} + \frac{\partial^2 \tilde{U}_r}{\partial z^2}\right], \tag{3}$$

θ-momentum equation

$$\frac{\partial \tilde{U}_\theta}{\partial t} + \tilde{U}_r \frac{\partial \tilde{U}_\theta}{\partial r} + \frac{\tilde{U}_\theta}{r}\frac{\partial \tilde{U}_\theta}{\partial \theta} + \frac{\tilde{U}_r \tilde{U}_\theta}{r} + \tilde{U}_z \frac{\partial \tilde{U}_\theta}{\partial z} + \frac{1}{r}\frac{\partial \tilde{P}}{\partial \theta}$$

$$= \frac{1}{\mathrm{Re}}\left[\frac{\partial^2 \tilde{U}_\theta}{\partial r^2} + \frac{1}{r}\frac{\partial \tilde{U}_\theta}{\partial r} - \frac{\tilde{U}_\theta}{r^2} + \frac{1}{r^2}\frac{\partial^2 \tilde{U}_\theta}{\partial \theta^2} + \frac{2}{r^2}\frac{\partial \tilde{U}_r}{\partial \theta}\right.$$

$$\left. + \frac{\partial^2 \tilde{U}_\theta}{\partial z^2}\right], \tag{4}$$

z-momentum equation

$$\frac{\partial \tilde{U}_z}{\partial t} + \tilde{U}_r \frac{\partial \tilde{U}_z}{\partial r} + \frac{\tilde{U}_\theta}{r}\frac{\partial \tilde{U}_z}{\partial \theta} + \tilde{U}_z \frac{\partial \tilde{U}_z}{\partial z} + \frac{\partial \tilde{P}}{\partial z}$$

$$= \frac{1}{\mathrm{Re}}\left[\frac{\partial^2 \tilde{U}_z}{\partial r^2} + \frac{1}{r}\frac{\partial \tilde{U}_z}{\partial r} + \frac{1}{r^2}\frac{\partial^2 \tilde{U}_z}{\partial \theta^2} + \frac{\partial^2 \tilde{U}_z}{\partial z^2}\right], \tag{5}$$

where r, θ, z are dimensionless coordinates and the normalization is based on the standard use of

$$r = \frac{\bar{r}}{a}, \quad z = \frac{\bar{z}}{a}, \quad t = \bar{t}\frac{U_w}{a}, \quad u = \frac{\bar{u}}{U_w}, \quad U = \frac{\bar{U}}{U_w},$$

$$p = \frac{\bar{p}}{\rho U_w^2}, \quad P = \frac{\bar{P}}{\rho U_w^2}, \quad \mathrm{Re} = \frac{U_w a}{\nu}, \quad l = \frac{L}{a}. \tag{6}$$

Here the overbar is used to denote a dimensional quantity.

III. STABILITY EQUATIONS

A. Linear instability theory

The linear instability principle consists of introducing a small sinusoidal disturbance into the Navier-Stokes equations in order to compute the range of unstable frequencies. A small perturbation $\breve{m}$ is hereby superimposed on the mean flowfield in each of its principal variables M. Assuming a total solution of the form $\tilde{M} = M + \breve{m}$, the small disturbances can be synthesized using normal mode decomposition *vis-à-vis*

$$\breve{u}_r = u_r(r)\exp[i(q\theta + \sigma z - \omega t)],$$

$$\breve{u}_\theta = u_\theta(r)\exp[i(q\theta + \sigma z - \omega t)],$$

$$\breve{u}_z = u_z(r)\exp[i(q\theta + \sigma z - \omega t)], \tag{7}$$

$$\breve{p} = p(r)\exp[i(q\theta + \sigma z - \omega t)],$$

where q is the tangential (i.e., azimuthal) wave number. Note that the complex amplitudes are only dependent on r. In the general case, σ and ω are complex and can be expressed by

$$\sigma = \sigma_r + i\sigma_i \quad \text{and} \quad \omega = \omega_r + i\omega_i. \tag{8}$$

Here, σ_r is the longitudinal wave number and ω_r is the circular frequency. While $-\sigma_i$ represents the growth rate in space, ω_i denotes the growth rate in time. Using the temporal disturbance argument, one may track the temporal growth of disturbances by setting $\sigma_i = 0$. Conversely, the spatial disturbance argument enables us to concentrate on the spatial

growth (with no temporal damping) by setting $\omega_i = 0$. According to available experimental evidence, it may be argued that the spatial theory is more suitable to treat this problem. At the outset, $\omega_r/(2\pi)$ will provide the dimensionless frequency of the disturbances with $f = \omega_r U_w/(2\pi a)$ representing the Hertzian frequency.

Equations (2)–(5) can be perturbed using $\tilde{U} = U + \breve{u}$ and $\tilde{p} = P + \breve{p}$. The resulting set is then expressible as function of the disturbance amplitudes by substitution of the normal mode transformations given by Eq. (7). After some algebra, one finds the linearized set

$$\frac{du_r}{dr} + \frac{u_r}{r} + iq\frac{u_\theta}{r} + i\sigma u_z = 0, \tag{9}$$

$$-i\omega u_r + U_r \frac{du_r}{dr} + u_r \frac{dU_r}{dr} + i\sigma U_z u_r + \frac{dp}{dr}$$

$$= \frac{1}{\mathrm{Re}}\left(\frac{d^2 u_r}{dr^2} + \frac{1}{r}\frac{du_r}{dr} - \frac{u_r}{r^2} - \frac{q^2}{r^2}u_r - \frac{2}{r^2}iqu_\theta - \sigma^2 u_r\right), \tag{10}$$

$$-i\omega u_\theta + U_r \frac{du_\theta}{dr} + \frac{U_r u_\theta}{r} + i\sigma U_z u_\theta + \frac{iq}{r}p$$

$$= \frac{1}{\mathrm{Re}}\left(\frac{d^2 u_\theta}{dr^2} + \frac{1}{r}\frac{du_\theta}{dr} - \frac{u_\theta}{r^2} - \frac{q^2}{r^2}u_\theta + \frac{2}{r^2}iqu_r - \sigma^2 u_\theta\right), \tag{11}$$

$$-i\omega u_z + U_r \frac{du_z}{dr} + u_r \frac{dU_z}{dr} + i\sigma U_z u_z + \frac{dU_z}{dz}u_z + i\sigma p$$

$$= \frac{1}{\mathrm{Re}}\left(\frac{d^2 u_z}{dr^2} + \frac{1}{r}\frac{du_z}{dr} - \frac{q^2}{r^2}u_z - \sigma^2 u_z\right). \tag{12}$$

This system encapsulates the interactions between mean components of velocity and the unsteady disturbances $\mathbf{u}(r)$ and $p(r)$. The implicit assumption is that while the steady (U_r, U_z) prescribe the motion and growth of unsteady waves, they themselves remain indifferent to the oscillations that they engender. In a recent study by Venugopal,[22] it was shown that fluctuations are highly sensitive to the mean flow distribution, particularly, along the axis. This reiterates the need to use the most suitable mean flow model for a given application. It also justifies the quest for refined mean flow models of rocket chambers, such as the ones incorporating the effects of grain taper[23] or compressibility.[24,25] In what follows, a careful set of boundary conditions is presented and discussed.

B. Vital boundary conditions

Equations (9)–(12) are second order in u_r, u_θ, and u_z; upon close examination, it may be determined that the total order is equal to 6 when $q \neq 0$ and reduces to 4 when $q = 0$ (see Sec. III C). Of the required boundary conditions, three may be inferred from the velocity adherence condition at the sidewall. As no slip is observed at leading order by the mean flow ingredient, the fluctuations must vanish at the sidewall

to avoid local interference. It should be noted that in combustion instability studies, two other types of fluctuations are considered: a purely acoustic, irrotational fluctuation $\hat{u}$ and a boundary driven, rotational fluctuation $\tilde{u}$ (see Griffond[26]). Unlike the hydrodynamic instability waves that evolve over short lengthscales due to mean flow breakdown, the acoustico-vortical $\hat{u}$ and $\tilde{u}$ travel at much higher speeds (comparable to the speed of sound) and over longer lengthscales. On the one hand, the parallel components of these two waves cancel each other at the surface independently of the hydrodynamic wave $\breve{u}$. On the other hand, their radial components do not vanish; they remain related to the oscillatory acoustic pressure $\hat{p}$ via the surface admittance function A_w and the wall injection Mach number M_w.[27,28] Using γ to represent the gas ratio of specific heats, the acoustic and vortical radial fluctuations at the sidewall are generally related through: $\hat{u}_r \propto -M_w A_w(\hat{p}/\gamma)$, $\tilde{u}_r \propto -M_w(\hat{p}/\gamma)$. Thus, while setting $u_\theta(1)=u_z(1)=0$ is prescribed by the no-slip condition at the wall, using $u_r(1)=0$ is an assumption that is required to obtain a solution. Accordingly, injection noise is entirely captured by the acoustico-vortical fluctuation; this enables us to set

$$u_r = u_\theta = u_z = 0 \quad \text{at} \quad r = 1. \tag{13}$$

Three conditions are still missing. To compensate, we expand the principal variables and substitute them into the linearized Navier-Stokes system. Suppression of singular terms is then used to extract the three desired constraints. Thus, using a polynomial expansion for the fluctuations,

$$u_r = \sum_{n=0}^{\infty} v_n r^n, \quad u_\theta = \sum_{n=0}^{\infty} w_n r^n,$$

$$u_z = \sum_{n=0}^{\infty} u_n r^n, \quad p = \sum_{n=0}^{\infty} p_n r^n \tag{14}$$

and, similarly, for the steady field,

$$U_z = f(z)\sum_{n=0}^{\infty} A_n r^n, \quad U_r = \sum_{n=0}^{\infty} B_n r^n, \quad U_\theta = 0, \tag{15}$$

these series may be substituted into Eqs. (9)–(12) and rearranged. Forthwith, singularities of order r^{-1} and r^{-2} are identified in the mass conservation and momentum equations. To ensure a uniformly valid outcome, these terms are set to zero. Collecting based on the orders in the chosen series expansion, one obtains

$$\text{System 1} \quad \begin{cases} v_0 + iqw_0 = 0, \\ (1+q^2)v_0 + 2iqw_0 = 0, \\ 2iqv_0 - w_0(1+q^2) = 0, \\ -q^2 u_0 = 0, \end{cases} \tag{16}$$

$$\text{System 2} \quad \begin{cases} 2v_1 + iqw_1 = -i\sigma u_0 \text{ from continuity at } O(1), \\ -q^2 v_1 - 2iqw_1 = 0, \\ 2iqv_1 - q^2 w_1 = -\text{Re}(iqp_0 + w_0 B_0), \\ u_1(1-q^2) = 0. \end{cases} \tag{17}$$

At this juncture, the full momentum equation is transformed into a gigantic system of equations that can be resolved to any order of accuracy depending on the summation integer n. This set is given by System 3 ($n \geq 0$):

$$(n+3)v_{n+2} + iqw_{n+2} + i\sigma u_{n+1} = 0, \tag{18}$$

$$[(n+2)^2 - (1+q^2)]v_{n+2} - 2iqw_{n+2} - \text{Re}(n+1)p_{n+1}$$
$$= \text{Re}\left[\left(\frac{\sigma^2}{\text{Re}} - i\omega\right)v_n + \sum_{j=0}^{n} \{[i\sigma fA_j + (j+1)B_{j+1}]v_{n-j} \right.$$
$$\left. + (n-j+1)B_j v_{n-j+1}\} \right], \tag{19}$$

$$2iqv_{n+2} + [(n+2)^2 - (1+q^2)]w_{n+2} - B_0 w_{n+1} - iq \text{ Re } p_{n+1}$$
$$= \text{Re}\left\{ \left(\frac{\sigma^2}{\text{Re}} - i\omega\right)w_n + \sum_{j=0}^{n} [B_{j+1} + i\sigma fA_j] \right.$$
$$\left. + (n-j+1)w_{n-j+1}] \right\}, \tag{20}$$

$$[(n+2)^2 - q^2]u_{n+2} - (\sigma^2 - i \text{ Re } \omega)u_n - i\sigma \text{ Re } p_n$$
$$= \text{Re} \sum_{i=1}^{n} \{[(f' + i\sigma f)A_j]u_{n+1} + (n-j+1)u_{n-j+1}B_j$$
$$+ f(j+1)A_{j+1}v_{n-j}\} \tag{21}$$

In this study, System 3 is not used but only reproduced for the sake of completeness. System 1 can be readily expressed in terms of velocity fluctuations. Depending on the tangential wave number, one can put, along the centerline,

$$q = 0 \rightarrow u_r(0) = u_\theta(0) = \frac{du_z}{dr}(0) = 0,$$

$$q = 1 \rightarrow \frac{du_r}{dr}(0) = \frac{du_\theta}{dr}(0) = u_z(0) = 0, \tag{22}$$

$$q \geq 2 \rightarrow u_r(0) = u_\theta(0) = u_z(0) = 0.$$

The three original boundary conditions due to no slip may now be supplemented by Eq. (22) to provide a complete set of auxiliary conditions for the velocity. To secure the pressure at $q=0$, one can substitute the findings in Eq. (22) back into Eq. (10). This enables us to deduce that $p'(0)=0$, where the prime is used to denote differentiation with respect to r. However, for $q \geq 1$, the first three equations of System 2 can be solved to obtain, along the centerline, the trivial set corresponding to $v_1 = w_1 = 0$ and $p_0 \equiv p(0) = 0$. We are thus compelled to apply a normalization condition for the pressure at the sidewall that does not affect the solution. Without loss in generality, we therefore set $p(1)=1$. By so doing, the pres-

sure magnitude becomes a normalizing factor for all remaining amplitudes.

C. Shooting procedure

Equations (9)–(12) can be rearranged and manipulated into six first-order ordinary differential equations (ODEs). Our approach follows precisely that of Malik.[29] Thus, u_r' is taken from mass conservation and inserted into the r-momentum equation. The latter is reduced to a first-order

ODE with two boundary conditions. The extra condition is used to secure convergence at the opposing boundary (here, we choose the sidewall as our shooting target). The six ODEs that must be solved form a linear set that can be expressed as

$$\frac{d[\mathbf{Z}]}{dr} = [\mathbf{C}][\mathbf{Z}], \quad [\mathbf{Z}] = \left\{ u_r, u_\theta, \frac{du_\theta}{dr}, u_z, \frac{du_z}{dr}, p \right\}^T. \quad (23)$$

The coefficient matrix $[\mathbf{C}]$ is prescribed by

$$[\mathbf{C}] = \begin{pmatrix} C_{11} & C_{12} & 0 & C_{14} & 0 & 0 \\ 0 & 0 & C_{23} & 0 & 0 & 0 \\ C_{31} & C_{32} & C_{33} & 0 & 0 & C_{36} \\ 0 & 0 & 0 & 0 & C_{45} & 0 \\ C_{51} & 0 & 0 & C_{54} & C_{55} & C_{56} \\ C_{61} & C_{62} & C_{63} & C_{64} & C_{65} & 0 \end{pmatrix};$$

$$\begin{cases} C_{11} = -\dfrac{1}{r}, \quad C_{12} = -\dfrac{iq}{r}, \quad C_{14} = -i\sigma, \quad C_{21} = 1, \\[2mm] C_{31} = -\dfrac{2iq}{r^2}, \\[2mm] C_{32} = \mathrm{Re}\left(-i\omega + \dfrac{U_r}{r} + i\sigma U_z\right) + \dfrac{1}{r^2}(q^2+1) + \sigma^2, \\[2mm] C_{33} = \mathrm{Re}\, U_r - \dfrac{1}{r}, \quad C_{36} = \mathrm{Re}\,\dfrac{iq}{r}, \end{cases} \quad (24)$$

and

$$C_{45} = 1, \quad C_{51} = \mathrm{Re}\, U_z', \quad C_{54} = \mathrm{Re}\left(i\sigma U_z - i\omega + \frac{\partial U_z}{\partial z}\right) + \frac{q^2}{r^2} + \sigma^2,$$

$$C_{55} = \mathrm{Re}\, U_r - \frac{1}{r}, \quad C_{56} = \mathrm{Re}\, i\sigma, \quad C_{61} = i\omega - U_r' - i\sigma U_z + \frac{U_r}{r} - \frac{1}{\mathrm{Re}}\left(\frac{q^2}{r^2} + \sigma^2\right), \quad (25)$$

$$C_{62} = iq\left(\frac{U_r}{r} - \frac{1}{\mathrm{Re}}\frac{1}{r^2}\right), \quad C_{63} = -\frac{1}{\mathrm{Re}}\frac{iq}{r}, \quad C_{64} = i\sigma U_r, \quad C_{65} = -\frac{1}{\mathrm{Re}} i\sigma.$$

This system admits a nontrivial solution by virtue of the pressure condition being nonhomogeneous. In order to expedite convergence, we find it instructive to discretize all terms in Z_i' using Chebyshev's spectral collocation method (see the Appendix).[30] At present, 200 collocation points are used in conjunction with Muller's root solving algorithm; this is a higher order representation of the secant method using three points to determine the zero of a quadratic interpolating curve.[31] The stencil density is found to be sufficient to insure the desired tolerance set at 10^{-9} in σ.[32] In marching forward, our dispersion relation linking all primitive variables and parameters takes the form of $f(\sigma, \omega, q, z, \mathrm{Re}, u_h) = 0$. Thus, in order to make headway, we choose for each tangential wave number q a certain frequency $\omega \equiv \omega_r$ at a fixed set of operating parameters (Reynolds number and headwall injection constant u_h). We then iterate at every spatial position of interest z on the complex σ until the target velocity amplitude u_r is made to vanish at the sidewall. This yields the amplitude vector $[\mathbf{Z}]$ in addition to the spatial growth rate $-\sigma_i$, and the wave number σ_r. From σ_r, one may calculate the spatial wavelength, $\lambda = 2\pi/\sigma_r$ and the axial speed of propagation (or phase velocity), $\dot{x} = \omega/\sigma_r$. After determining our first two σ_r

values, we linearly extrapolate for the subsequent initial guess. Throughout this simulation, we fix the Reynolds number at 5000 and u_h for the application at hand. At this level of sidewall injection, it is universally accepted that inviscid conditions will prevail to the extent that our steady-state model becomes an accurate representation of the incompressible core flow described by Eq. (1). For solid rocket motor applications, one may contemplate an order of magnitude increase in the sidewall Reynolds number above 5000; under these auspices, compressibility effects may become quite important, depending on the length of the motor. The criteria that establish the error in using Eq. (1) are presented in a paper by Majdalani.[24] Accordingly, one may need to use, at sufficiently high wall Mach numbers, a compressible mean flow solution in conjunction with the compressible Navier-Stokes equations to re-address this problem.

The second parameter that is left invariant for a given simulation is the tangential wave number q. Thus, for each frequency ω, we march in space up to the point prescribed by $z = 20$. The axial extent is covered in equal spatial increments of 0.1. After completing each sweep, we then increase the frequency by a variable amount: at low ω, we use a fine step

TABLE I. Eigenvalues of the Taylor-Culick profile at $\omega=80$, $z=10$, $q=0$, and Re$=4500$.

Mode	Published data (Ref. [4])		Present solution	
	σ_r	σ_i	σ_r	σ_i
1	6.095 294 565 6	−1.078 799 814 0	6.095 294 572 4	−1.078 799 810 1
2	3.326 428 536 6	−0.109 552 558 9	3.326 428 538 0	−0.109 552 558 1
3	2.601 322 331 0	0.132 287 031 5	2.601 322 355 4	0.132 283 002 5

size of 1 to capture the critical frequency at the nose-tip of the iso-n curves; these are defined and illustrated in the next section. The step size is then increased to 5 and 10 as we approach linear behavior in the iso-n curves. The maximum frequency we explore depends on the headwall injection constant. For $u_h=0.5$, our maximum frequency reaches 175, whereas for $u_h=50$ we find it necessary to raise the bar to 800. The highest ω that we investigate is the one that enables us to capture the most amplified value of n at $z=15$. This typically coincides with the iso-n curve reaching an amplification factor of $n=11$. Based on existing experimental data with no headwall injection, transition to turbulence takes place between $n=7$ and 9 according to stability theory[2] and experiments.[33] For $u_h=0.5$, a similar behavior is expected. It can thus be argued that any evolution beyond $n=9$ may no longer observe linear instability theory or help to delimit the unstable domain. More experimental work with headwall injection is therefore required to substantiate further refinement to this analysis.

IV. RESULTS AND DISCUSSION

A verification of the numerical procedure used to solve Eq. (23) subject to Eq. (22) can be carried out by applying our algorithm to the special case of $u_h=0$. Results are illustrated in Table I for the first three eigenvalues that are precipitated by the numerical routine. These so-called eigenmodes are compared to published data in descending order of criticality.[4] Note the favorable agreement (in five to ten significant digits) between the present eigenvalues and those obtained by Griffond and Casalis.[4] In the remainder of this work, only the most critical eigenmode will be considered for each set of parameters.

From a practical standpoint, we recognize that the effect of the headwall injection constant u_h must be carefully investigated alongside the effect of varying the tangential wave number. The graph for the iso-n factor is first computed for four cases involving $u_h=0.5$, Re$=5000$, and $q=0,1,2,3$; these cases represent the first four tangential fluctuation modes of an SRM with headwall burning (see Fig. 2). The iso-n factors represent the spatial amplification of the flow and can be computed from fixed values of Re, q, z, and ω. The amplitude of the wave A is calculated by integrating the local amplification growth rate $(-\sigma_i)$ as described in Eq. (26): the value of $z_0(\omega)$, the first axial position where marginal stability is reached, depends on these fixed values via

$$A(z,\omega)=A_0 e^n \quad \text{with} \quad n(z,\omega)=-\int_{z_0(\omega)}^{z}\sigma_i(x,\omega)\mathrm{d}x. \quad (26)$$

Here, A_0 represents the last stable amplitude along the neutral curve prescribed by $n=0$. The iso-n graph in Fig. 2 provides several useful flow-related features.

First, one may recognize the unstable region to be enclosed within the classic L-shaped boundary. The vertical range of unstable frequencies increases in the streamwise direction. By the same token, for each specific frequency above the horizontal branch of the curve, the n-factor increases as the flow approaches the downstream end of the chamber. Second, the axial position of the most amplified frequency seems to change very gradually with successive increases in q. Only a minor shift in the neutral curve is detected. Third, flow stability at a spatial position seems to increase at higher wave numbers as a result of the curves shifting in the positive z direction. This point can be seen more clearly by comparing the neutral curves at several tangential wave numbers.

Figure 3 displays the neutral curves of Fig. 2 for $q=0,1,2,3$. These represent the lines along which the flow begins to destabilize. It can be seen that the largest unstable frequency at a given z is nearly the same at all tangential wave modes. This can be attributed to the overlapping of the upper branch of the neutral curves past $z=6$. For a sufficiently high frequency, the neutral curves at different wave numbers begin to overlap to the extent of becoming nearly imperceptible; this duplicitous behavior is confounding to the extent of making it difficult to isolate modes at a given frequency during experimental measurements.[2,33] On the other hand, due the continual spatial shifting of the lower branch in the streamwise direction (as the wave number is increased), the $q=0$ case appears to be the most amplified. In fact, the two lowest modes ($q=0,1$) are nearly indiscernible; this trend can make them difficult to decipher from experimental measurements.

Note that a double shooting technique has been developed to specifically calculate the lines along which both σ_i and ω_i vanish simultaneously. This approach serves a dual purpose. First, it enables us to directly and expeditiously locate the neutral points, thus obviating the need to sweep horizontally across the domain to tag each of the neutral points individually. Second, as a consequence to the first, a larger number of points can be collected in a shorter period of time. This improves our resolution by permitting the use
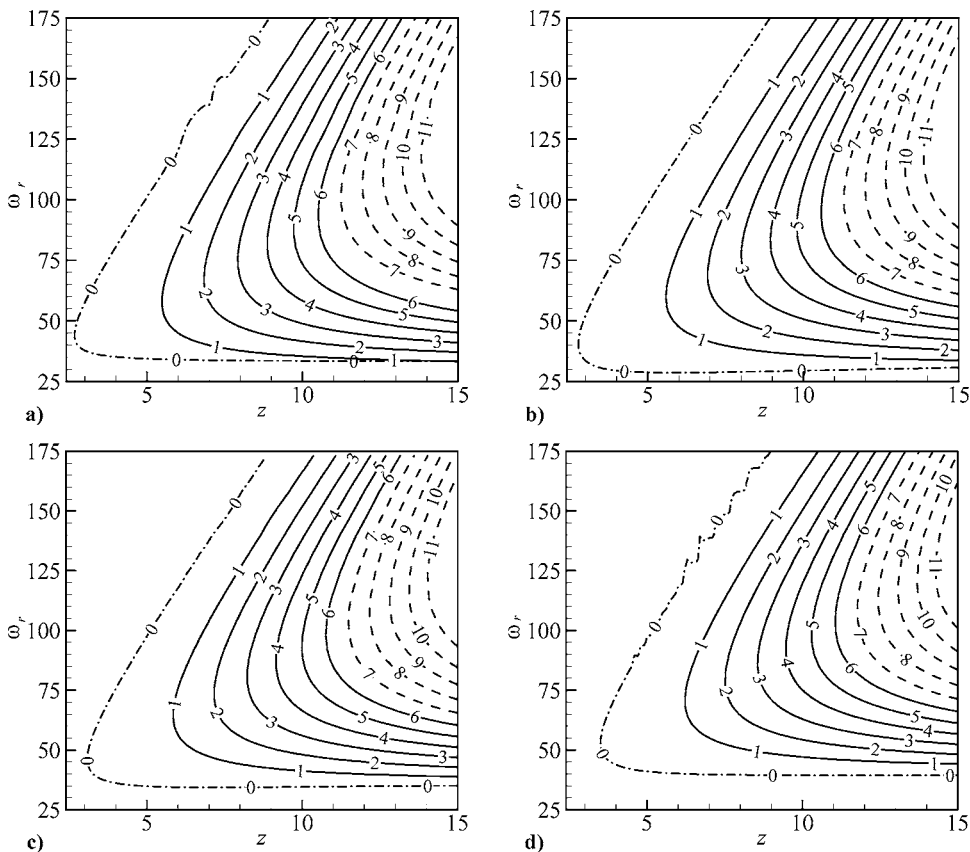
FIG. 2. Iso-n factors for Re=5000 and u_h=0.5. Results are shown in (a) through (d) for q=0,1,2,3.

of finer increments and, thereby, deducing smoother curves.

Another observation that can be made based on Fig. 3 is that the flow is always stable below a certain frequency; in that respect, each neutral curve shows a tip that depends on the fixed parameters, Re, q, and u_h. For example, in the most dominant cases of q=0 and 1, the flow is always stable below a threshold frequency of ω_r=28.5; the critical values (i.e., the tips of the neutral curves) are captured at $z \simeq 2.6$ and 2.7 with a common ω_r=43 and $\sigma_r \simeq (6.40, 6.23)$, respectively. For q=2, the frequency above which instability starts increases to ω_r=34; this occurs at ω_r=47, $z \simeq 3$, and $\sigma_r \simeq 6.67$. Similar trends depicting an upward shift in frequency

FIG. 3. Neutral curves for different values of q at Re=5000 and u_h=0.5.

are reported with further increases in the wave number. This behavior confirms the q=0 case as being the most critical.

To examine the effect of the injection headwall constant, neutral curves for different values of u_h are processed and plotted in Fig. 4(a). Clearly, as u_h increases, the flow becomes gradually more unstable; the corresponding neutral curves steadily shift upstream. The critical value, in this case, starts at the headwall injection point when the injection constant reaches $u_h \simeq 3.168$.

When $u_h > 3.168$, there will exist a range of frequencies for which the flow becomes unstable starting at the injection point itself (z=0); the spectrum of frequencies widens with further departures from u_h=3.168. One should point out that the critical value of u_h varies with the tangential wave number. However, the q=0 case shown here remains the most critical.

As the headwall-to-sidewall injection ratio becomes large [(see Fig. 4(b)], the flow streamlines start to resemble those of a circular-port hybrid rocket chamber.[21] By way of illustration, two values of u_h, (10,50), are selected. Here, too, the range of unstable frequencies is seen to expand significantly at higher headwall injection rates. It may be helpful to mention that the lowest frequency where the flow starts to amplify (i.e., the frequency where the lower, horizontal segment of the neutral curve starts to swerve) is weakly sensitive to u_h [see Fig. 4(a)] In contrast, the tip location and the highest unstable frequency are strongly affected by u_h. The tip moves upstream and the highest frequency increases as u_h is augmented. Additionally, as illustrated previously in Fig.
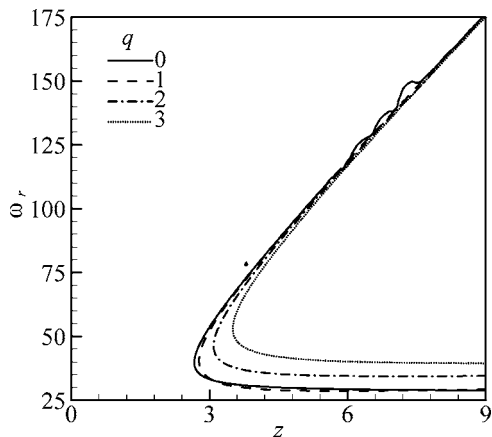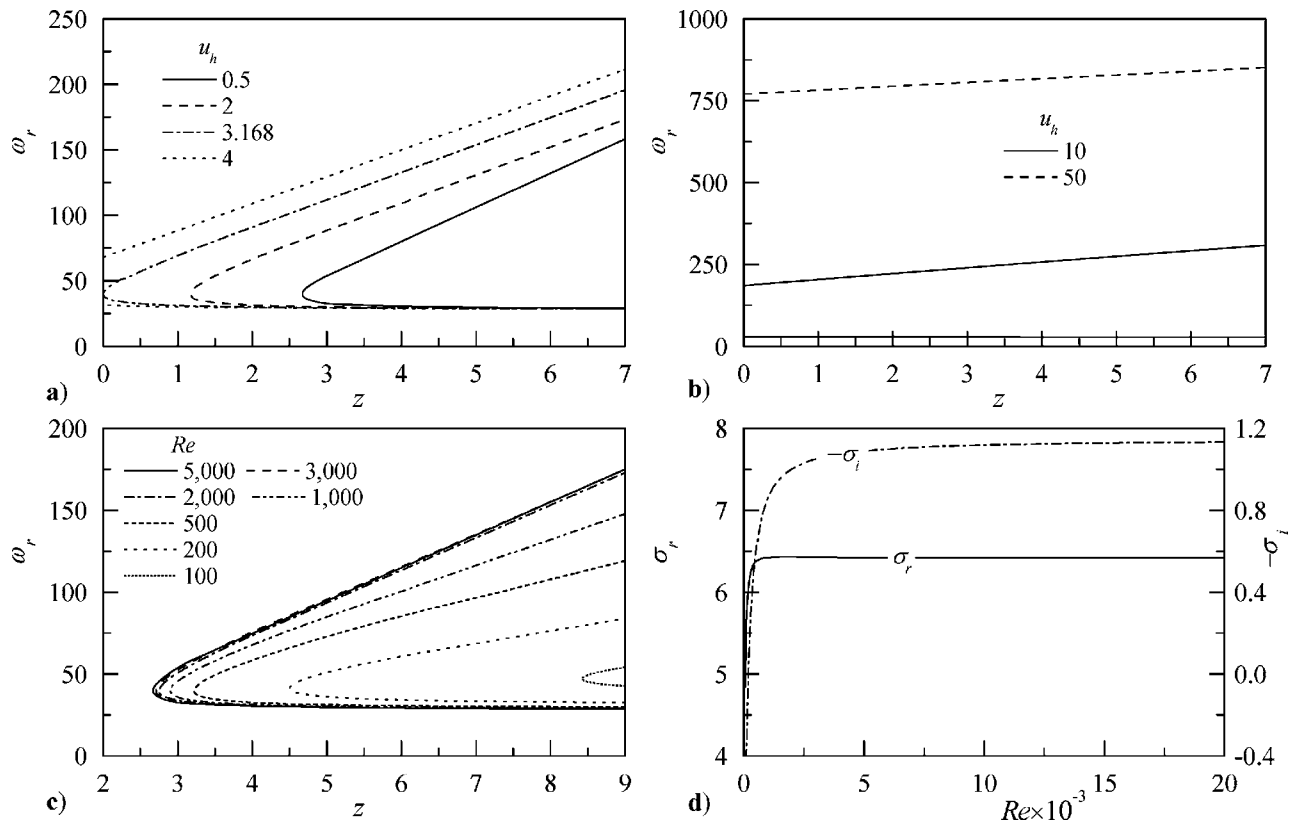
FIG. 4. Using Re=5000 and $q=0$, we present the neutral curves for (a) simulated SRM with headwall burning and (b) simulated hybrid rocket engine. In (c), the effect of Reynolds number on the spatial shift in stability is illustrated for a simulated SRM with headwall burning ($q=0$ and $u_h=0.5$). For the same case, the behavior of the streamwise wave number is plotted in (d) over a wide range of Reynolds numbers and fixed values of $\omega=80$ and $z=9$.

3, these features are dependent on the tangential wave number q. The impact of u_h on controlling the tip and the upper branch of the neutral curve is clearly seen in Fig. 4(b); accordingly, the flow regains stability at $\omega_r \geq (185,770)$ for $u_h=(10,50)$, respectively.

Another interesting behavior that can be captured is the effect of Reynolds number on motor stability. To that end, Fig. 4(c) is used to illustrate the effect of Re on the position and size of the neutral curve. These determine the first abscissa at which instability can be experienced and the range of amplified frequencies, respectively. For Re ≥ 2000, a clustering in the neutral curves can be seen; this weak sensitivity to the Reynolds number marks the beginning of inviscid behavior.

As shown in Fig. 4(d), the longitudinal wave number and the amplification rate $(\sigma_r, -\sigma_i)$ become independent of Re above a certain threshold value; namely, one that is often termed the critical Reynolds number Re_c. Essentially, both σ_r and $-\sigma_i$ reach their asymptotic values when the Reynolds number exceeds Re_c. This value represents the starting point at which inviscid behavior prevails. For the special case shown in Fig. 4(d), the critical value of Reynolds number is found to be $Re_c \simeq 2225$. Note that the wave number tends to the inviscid limit faster than the growth rate and that the deviation in σ_i is quite minute (cf. right-hand scale). For Re ≥ 5000, no change may be observed and this justifies its adoption in the present analysis.

In the process of investigating the amplitudes of distur-

bances at various frequencies and spatial stations, we have uncovered an acoustic instability-like phenomenon, namely, one with potentially serious implications. We have identified the presence of rising amplitudes over a short range of frequencies for the hybrid rocket model at the zeroth tangential mode. This is illustrated in Fig. 5, where the spectrum of wave amplitudes is shown both in waterfall and planar formats. We remind the reader that the amplitudes here depend on the wall pressure being set equal to unity. In Fig. 5(a), the increasing pressure resurgences are displayed at discrete axial positions over a wide range of frequencies. The same curves are overlaid in Fig. 5(b) to help in tracking their relative evolution with respect to both frequencies and abscissas. Interestingly, these peaks coincide with the points at which $-\sigma_i$ is largest. From the design standpoint, the frequencies that are accompanied by intense surges in pressure and velocity amplitudes constitute the most detrimental and, thereby, undesirable group. As shown on the graph, the most excited frequencies are detected between $\omega=387$ and 415 at $z=(2,4)$, near the headwall (where the LNP approach becomes fragile). Spatially, their peaks are seen to slowly drift downstream while their oscillatory amplitudes are generally diminishing. Being capable of exceeding the burst pressure of the rocket motor case, the dimensional frequencies associated with $\omega=[387,415]$ must be judiciously avoided in hybrid rocket design. In passing, it may be interesting to note the qualitative resemblance between Fig. 5(a) and experimental spectra obtained when acoustic instabilities are de-
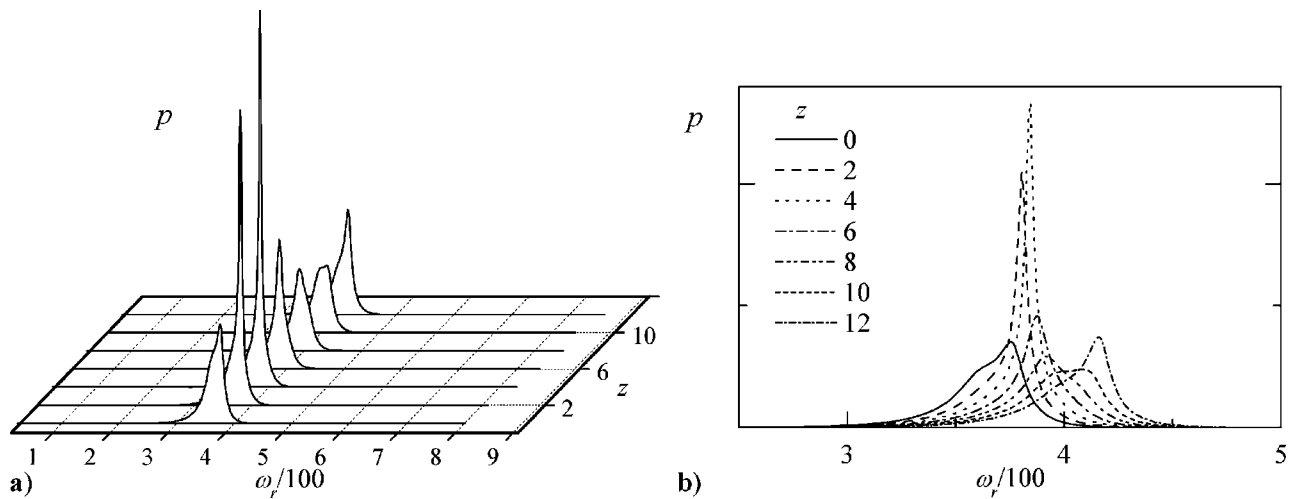
FIG. 5. Spectrum of pressure amplitudes versus frequencies along a circular radius of $r=0.5$ and increasing distance from the headwall. Note the presence of large bumps in the pressure (and similarly in the unsteady radial and streamwise velocities) over a range of undesirable frequencies. As usual, we use Re $=5000$ to mimic inviscid behavior, $u_h=50$ for a hybrid rocket model, and $q=0$ for the most unstable scenario.

tected in rockets. We also note that the same level of scrutiny has been directed at higher tangential modes but only to recover damped amplitudes; aside from $q=0$, no other modes are found to be susceptible to this phenomenon. When the headwall injection is reduced to $u_h=0.5$, a similar phenomenon is observed except that the growth is spatially delayed and spread over wider and dissimilar frequency ranges (see Fig. 6). It is most pronounced near $z=10$ and spread over a range of lower frequencies, specifically, $\omega=[93.8, 163.5]$. The fact that the amplified frequency changes quite noticeably with z reduces the overall propensity to resonance. We thus realize that the unsafe frequencies diminish at lower headwall injection rates for which a more globally stable flowfield is obtained.

V. CONCLUSIONS

In this article we have applied linear spatial theory to characterize the hydrodynamic instability of solid and hybrid rockets with headwall injection. We have determined that headwall injection plays a destabilizing role considering that the range of unstable frequencies is broadened with succes-

sive increases in u_h. This is also accompanied by an upstream translation of the critical abscissas and attendant shifting of the neutral curves.

By using the extended Taylor-Culick profile proposed by Majdalani and Vyas,[21] we are able to study the effect of headwall injection on stability. By using $u_h=0.5$, our model is capable of mimicking the core flow in long solid rocket motors with reactive forward closure. Such motors are only slightly more unstable than SRMs with inert headwalls. When u_h is increased to 3.168, the most critical point along the neutral curve (i.e., the tip) is shifted upstream to the extent of reaching the headwall (by contacting the frequency axis). Thus, at $z=0$ and $\omega=40$, the flow becomes unstable at the injection point. Further increases in u_h cause the concave portion of the neutral curve to fall behind the frequency axis, namely, in the negative z domain. Under such conditions, the flow becomes unstable even at $z=0$ over an increasing range of frequencies. This range is bracketed by the intersection of the neutral curve and the frequency axis. The forward truncation of the neutral curve prevents us from calculating the amplification n-factors.
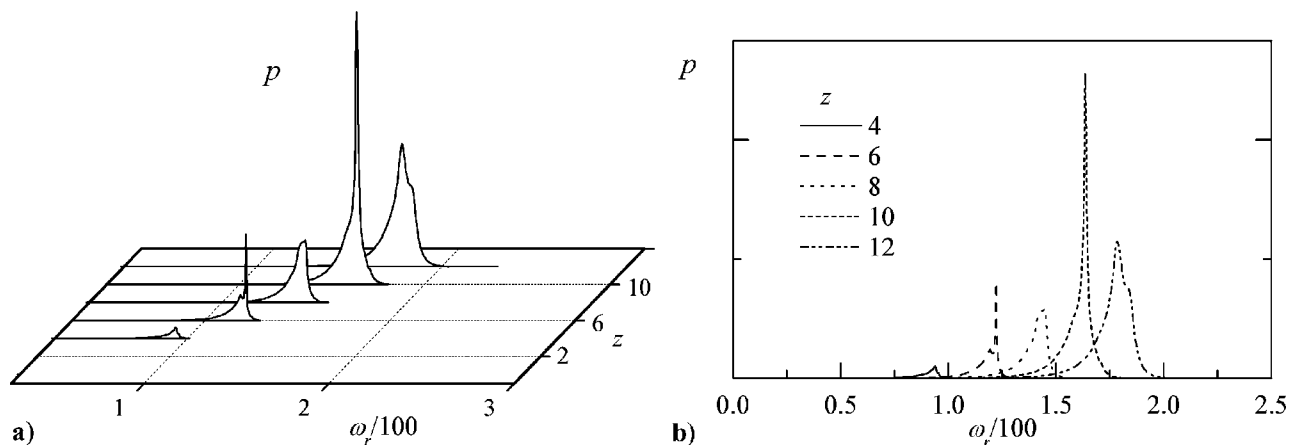

FIG. 6. Same as previous except for $u_h=0.5$ corresponding to a solid rocket model with reactive headwall.

One of the most interesting aspects of this study is the discovery of a range of frequencies at the zeroth tangential mode along which enormous surges in pressure amplitudes are possible. These large excursions in pressure signal the presence of a pronounced resonant-like phenomenon that is reminiscent of an acoustic instability response. The most excited frequencies where the engine experiences the most appreciable excursions are detected in the vicinity of the headwall. These appear to slowly decrease and shift away with successive decreases in headwall injection. As we march downstream we observe a quasi-steady depreciation in pressure amplitudes. From a practical standpoint, these resurging amplitudes may be the most relevant to the designer; when the amplification rates are high, they do not necessarily have a bearing on the mean pressure unless the corresponding wave amplitudes are large. It is interesting that, as the headwall injection velocity is increased, the character of the solution approaches that of parallel mean flow motion; specifically, the frequencies associated with pressure resurgences become nearly uniform; i.e., $\forall z$. This may be highly conducive to resonance by way of coupling with chamber acoustics whose frequencies are always independent of z. In future work, we plan to further investigate this phenomenon in the hope of unraveling additional connections with acoustic instability theory, especially in what regards wave amplitudes and energy accumulation rates.

ACKNOWLEDGMENTS

APPENDIX: DISCRETIZATION

Discretization of the disturbed system is based on a spectral collocation method.[30] Accordingly, we define $\xi = 2r - 1 \in [-1, 1]$ and choose T_N to be the Nth-order Chebyshev polynomial. The $N+1$ collocation points are

$$\xi_i = \cos\left(\frac{\pi i}{N}\right), \quad i = 0, \dots, N. \tag{A1}$$

Equation (A1) enables us to calculate the so-called Gauss-Lobatto points. Subsequently, the amplitude function ψ can be interpolated using the polynomial form $\psi(\xi) = \Sigma \lambda_i \psi(\xi_i)$, where λ_i denotes a Lagrangian multiplier

$$\lambda_i(\xi) = \left(\frac{1 - \xi_i^2}{\xi - \xi_i}\right)(-1)^{i+1}\frac{T_N'}{N^2 c_i}. \tag{A2}$$

Here, T_N' is the derivative of Nth Chebyshev polynomial. The $N+1$ discrete values of $\psi_i = \psi(\xi_i)$ are originally unknown. Their accuracy depends on the size of N. As ψ is a solution of a differential problem, a tacit relation can be obtained between the derivative ψ' and ψ itself. After some algebra, one finds

$$D_{ik} = \frac{c_i}{c_k}\frac{(-1)^{k+i}}{(\xi_i - \xi_k)}, \quad i \neq k; \quad D_{ii} = -\frac{\xi_i}{2(1 - \xi_i^2)},$$

$$i = 1, \dots, N-1; \quad D_{00} = -D_{NN} = \frac{2N^2 + 1}{6}, \tag{A3}$$

where $c_0 = c_N = 2$, $c_i = 1$, $i = 1, \dots, N-1$, and the discretized equations can be written as

$$\frac{d\psi}{d\xi}(\xi_i) = \sum_{k=0}^{N} D_{ik}\psi_k, \tag{A4}$$

where ψ represents the amplitude components; namely, $\psi = (u_r, u_\theta, u_z, p)$.

[1] G. Casalis, G. Avalon, and J.-P. Pineau, "Spatial instability of planar channel flow with fluid injection through porous walls," Phys. Fluids **10**, 2558 (1998).

[2] J. Griffond, G. Casalis, and J.-P. Pineau, "Spatial instability of flow in a semiinfinite cylinder with fluid injection through its porous walls," Eur. J. Mech. B/Fluids **19**, 69 (2000).

[3] J. Griffond and G. Casalis, "On the nonparallel stability of the injection induced two-dimensional Taylor flow," Phys. Fluids **13**, 1635 (2001).

[4] J. Griffond and G. Casalis, "On the dependence on the formulation of some nonparallel stability approaches applied to the Taylor flow," Phys. Fluids **12**, 466 (2000).

[5] G. I. Taylor, "Fluid flow in regions bounded by porous surfaces," Proc. R. Soc. London **234**, 456 (1956).

[6] F. E. C. Culick, "Rotational axisymmetric mean flow and damping of acoustic waves in a solid propellant rocket," AIAA J. **4**, 1462 (1966).

[7] G. Avalon, G. Casalis, and J. Griffond, "Flow instabilities and acoustic resonance of channels with wall injection," AIAA Paper 98-3218, Cleveland, OH, 1998.

[8] A. S. Berman, "Laminar flow in channels with porous walls," J. Appl. Phys. **24**, 1232 (1953).

[9] V. N. Varapaev and V. I. Yagodkin, "Flow stability in a channel with porous walls," Izv. Akad. Nauk SSSR, Mekh. Zhidk. Gaza **4**, 91 (1969).

[10] R. A. Beddini, "Injection-induced flows in porous-walled ducts," AIAA J. **24**, 1766 (1986).

[11] R. A. Beddini and T. A. Roberts, "Turbularization of an acoustic boundary layer on a transpiring surface," AIAA J. **26**, 917 (1988).

[12] Y. Lee and R. A. Beddini, "Acoustically-induced turbulent transition in solid propellant rocket chamber flowfields," AIAA Paper 99-2508, Los Angeles, CA, 1999.

[13] Y. Lee and R. A. Beddini, "Effect of solid rocket chamber pressure on acoustically-induced turbulent transition," AIAA Paper 2000-3802, Huntsville, AL, 2000.

[14] G. Avalon and P. Comas, "Simulative study of the unsteady flow inside a solid propellant rocket motor," AIAA Paper 91-1866, Sacramento, CA, 1991.

[15] F. Vuillot and G. Avalon, "Acoustic boundary layer in large solid propellant rocket motors using Navier-Stokes equations," J. Propul. Power **7**, 231 (1991).

[16] F. Vuillot, "Vortex-shedding phenomena in solid rocket motors," J. Propul. Power **11**, 626 (1995).

[17] D. Couton, S. Doan-Kim, and F. Vuillot, "Numerical simulation of vortex-shedding phenomenon in a channel with flow induced through porous wall," Int. J. Heat Fluid Flow **18**, 283 (1997).

[18] B. Ugurtas, G. Avalon, N. Lupoglazoff, and F. Vuillot, "Numerical computations of hydrodynamic instabilities inside channels with wall injection," AIAA Paper 99-2505, Los Angeles, CA, 1999.

[19] B. Ugurtas, G. Avalon, N. Lupoglazoff, F. Vuillot, and G. Casalis, "Stability and acoustic resonance of internal flows generated by side injection," in *Solid Propellant Chemistry, Combustion, and Motor Interior Ballistics*, edited by V. Yang, T. B. Brill, and Wu-Zhen Ren, in Progress in Astronautics and Aeronautics Vol. 185 (American Institute of Aeronautics and Astronautics, Weston, VA, 2000), pp. 823–836.

[20] Y. Fabignon, J. Dupays, G. Avalon, F. Vuillot, N. Lupoglazoff, G. Casalis, and M. Prévost, "Instabilities and pressure oscillations in solid rocket mo-

tors," Aerosp. Sci. Technol. **7**, 191 (2003).

[21] J. Majdalani and A. B. Vyas, "Inviscid models of the classic hybrid rocket," AIAA Paper 2004-3474, Fort Lauderdale, FL, 2004.

[22] P. Venugopal, "Direct numerical simulation of turbulence in a model solid rocket motor," Ph.D. dissertation, University of Illinois at Urbana-Champaign, 2003.

[23] T. Saad, O. C. Sams, and J. Majdalani, "Rotational flow in tapered slab rocket motors," Phys. Fluids **18**, 103601 (2006).

[24] J. Majdalani, "On steady rotational high speed flows: the compressible Taylor-Culick profile," Proc. R. Soc. London, Ser. A **463**, 131 (2007).

[25] B. A. Maicke and J. Majdalani, "The Compressible Taylor Flow in slab rocket motors," AIAA Paper 2006-4957, Sacramento, CA, 2006.

[26] J. Griffond, "Receptivity and aeroacoustic resonance in channels with blowing walls," Phys. Fluids **14**, 3946 (2002).

[27] F. E. C. Culick, "Calculation of the admittance function for a burning surface," Astronaut. Acta **13**, 221 (1967).

[28] F. E. C. Culick, "A review of calculations for unsteady burning of a solid propellant," AIAA J. **6**, 2241 (1968).

[29] M. R. Malik, "Numerical methods for hypersonic boundary layer stability," J. Comput. Phys. **86**, 376 (1990).

[30] W. S. Don and A. Solomonoff, "A boundary value problem with multiple solutions from the theory of laminar flow," SIAM J. Sci. Comput. (USA) **16**, 1253 (1995).

[31] D. Prasad, *Introduction to Numerical Analysis*, 2nd ed. (Alpha Science International, Harrow, UK, 2005).

[32] E. M. Abu-Irshaid, J. Majdalani, and G. Casalis, "Hydrodynamic instability of the bidirectional vortex," AIAA Paper 2005-4531, Tucson, AZ, 2005.

[33] R. S. Brown, R. Dunlap, S. W. Young, and R. C. Waugh, "Vortex shedding as a source of acoustic energy in segmented solid rockets," J. Spacecr. Rockets **18**, 312 (1981).